

# Group Conductivity and Nonadiabatic Born Effective Charges of Disordered Metals, Warm Dense Matter and Hot Dense Plasma

Vidushi Sharma<sup>1,2,3,\*</sup> and Alexander J. White<sup>1,†</sup>

<sup>1</sup>Theoretical Division, Los Alamos National Laboratory, Los Alamos, NM 87545, USA

<sup>2</sup>Center for Nonlinear Studies, Los Alamos National Laboratory, Los Alamos, NM 87545, USA

<sup>3</sup>Applied Materials and Sustainability Sciences, Princeton Plasma Physics Laboratory, Princeton, NJ 08540-6655, USA

(Dated: August 30, 2024)

The average ionization state is a critical parameter in plasma models for charged particle transport, equation of state, and optical response. The dynamical or nonadiabatic Born effective charge (NBEC), calculated via first principles time-dependent density functional theory, provides exact ionic partitioning of bulk electron response for both metallic and insulating materials. The NBEC can be trivially transformed into a “group conductivity”, *i.e.*, the *electron* conductivity ascribed to a subset of ions. We show that for disordered metallic systems, such as warm dense matter (WDM) and hot dense plasma, the static limit of the NBEC is different from the average ionization state, but that the ionization state can be extracted from the group conductivity even in mixed systems. We demonstrate this approach using a set of archetypical examples, including cold and warm aluminium, low- and high- density WDM carbon, and a WDM carbon-beryllium-hydrogen mixture.

Warm dense matter (WDM) physics is key to many complex systems [1–3]. WDM is generated in the initial phases of an inertial confinement fusion experiment and forms the cores of planetary systems, ice giants and exoplanets [4–7]. Its theoretical description poses a challenge. Nearly every analytical model for materials properties in WDM or hot dense plasma (HDP) regimes involves the average ionization state, *i.e.*, the effective or partial charge of ions,  $Z_{\text{eff}}$  [8–11]. This includes electronic conductivity and thermal conductivity [12–16], electron-ion relaxation rates [17], X-ray scattering [18–21], charged particle stopping power [22–29], inverse Bremsstrahlung absorption [30–32], as well as equation of state [33–35], ionic transport properties [36, 37], and multi-species mixing rules [38–43].

In a weakly coupled plasma regime where degeneracy effects and ion correlations are negligible, the Saha model can be applied [44, 45]. For highly degenerate plasmas, the Thomas-Fermi model can be utilized but it does not account for discrete electronic levels [44, 46]. When strong ion correlations emerge at liquid or solid densities, *ab initio* multi-atom quantum mechanical simulations are imperative for determining  $Z_{\text{eff}}$ . This is challenging because  $Z_{\text{eff}}$  is not a well-defined observable, *i.e.*, there is no unique quantum operator which defines it.

There exists a gamut of charge partitioning schemes frequently employed in quantum chemistry, such as Mulliken [47], Bader [48], Hirshfeld [49], etc [50]. However, in disordered metals and in the WDM regime, wherein a significant number of electrons behave as “nearly-free”, these assignments become substantially more difficult and arbitrary, with a more homogeneous electron density and a larger contribution from high energy electrons,

*i.e.*, a basis dependence [51]. An alternative approach is to extract  $Z_{\text{eff}}$  from well-defined observables, *e.g.*, the electrical conductivity [52, 53] or the electronic density of states [54, 55]. However, these are *bulk* properties of the system, not atomically resolved. This prevents the determination of  $Z_{\text{eff}}$  distributions, or in the case of multi-component mixtures, the contribution from different elements. In this letter, we show that by exploiting the nonadiabatic forces on atoms we can extract both an atomistically resolved conductivity  $\sigma^G$  as well as an element-specific average charge,  $Z_{\text{eff}}^G$ .

The static *Born* (or transverse [56]) effective charge tensor (BEC,  $\hat{Z}_a^*$ ) is a second-order linear response property and a well-defined quantum observable [57]. It is defined as the negative of the change in the atomic force vector ( $\mathbf{F}^a$ ) with respect to an applied electric field vector ( $\mathbf{E}$ ), or equivalently, the change in the electronic polarization vector ( $\mathbf{P}$ ) with respect to an atomic displacement vector ( $\delta\mathbf{R}^a$ ) shifted by the bare nuclear charge ( $Z_a$ ):

$$\hat{Z}_a^* = -\frac{\partial \mathbf{F}_a}{\partial \mathbf{E}} = Z_a \hat{I} + \frac{\partial \mathbf{P}}{\partial \mathbf{R}^a}, \quad (1)$$

where  $\hat{I}$  is the identity matrix, and ‘*a*’ indexes the atom. For gapped materials, *i.e.*, insulators and semiconductors,  $\hat{Z}_a^*$  can be calculated via perturbation theory [58]. However, for metallic systems and doped semiconductors, the electric polarization is ill-defined in the static limit [59], and the static BEC has often been assumed to be ill-defined as well [60]. Recently, Dreyer, Coh, and Stengel (DCS) used the concept of *nonadiabatic* or *dynamical* BEC (NBEC,  $\hat{Z}_a^*(\omega + i\gamma)$ ), to extend BEC to metals [61]. Here  $\omega$  is the frequency of the perturbing field,  $\gamma$  is a small positive number required due to finite simulation times and system sizes. Upon taking the zero-frequency limit,  $\omega \rightarrow 0$ , the usual BEC is recovered [61]. Wang *et al.* provided a phenomenological framework for computing the finite-frequency NBEC for crystalline sys-

\* vidushi@princeton.edu

† alwhite@lanl.gov

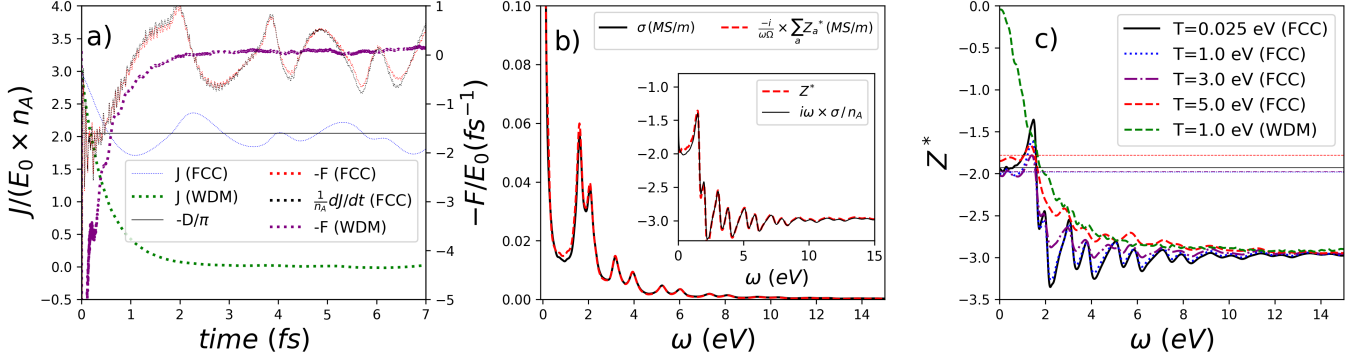


FIG. 1. Aluminium at solid-state density  $\rho = 2.7 \text{ g/cm}^3$ . *a*) fcc at  $k_B T = 0.025 \text{ eV}$ , disordered (WDM) at  $k_B T = 1.0 \text{ eV}$ , on the vertical axes: (left)  $J$  is scaled such that the signal is proportional to the number of electrons per atom, (right) negative of the force is scaled by  $E_0$  yielding units of inverse time. Here,  $-D/\pi$  is plotted for the fcc case. *b*) Current- and force- derived conductivity (Eq. (5)), and the current- and force- derived average NBEC (inset, Eq. (3)). *c*) NBEC for fcc geometry at  $k_B T = \{0.025, 1.0, 3.0, 5.0\} \text{ eV}$ , and disordered (WDM) phase at  $k_B T = 1.0 \text{ eV}$ .

tems using Time-Dependent Density Functional Theory (TDDFT) [62, 63].

The DCS sum rule states that the sum of all NBEC's, divided by the cell volume  $\Omega$ , yields the ‘‘Drude Weight’’,

$$\frac{1}{\Omega} \sum_a \hat{Z}_a^*(0 + i\gamma)|_{\gamma \rightarrow 0} = -\frac{\hat{D}}{\pi}, \quad (2)$$

establishing a generalization of the acoustic sum rule applicable to both insulators ( $\hat{D} = 0$ ) and metals ( $\hat{D} \neq 0$ ) [64]. *This* Drude weight is the ‘‘truly-free’’ electron contribution to the electrical conductivity tensor ( $\hat{\sigma}$ ). It is proportional to the number of electrons that, having ‘‘high inertia’’ or weak-coupling to the ion lattice, do not respond to a rigid translation of the ionic sublattice or equivalently do not relax to their ground-state after being kicked by an instantaneous uniform electric field [65, 66]. However, due to electron relaxation in disordered systems,  $\hat{D} \rightarrow 0$  and thus  $\sum_a \hat{Z}_a^*(\omega)|_{\omega \rightarrow 0} \rightarrow 0$  as well, even in gap-less electronically-conducting systems such as disordered metals, WDM, or HDP. The average of the diagonal of the NBEC tensor,  $\bar{Z}^*(\omega \rightarrow 0)$ , cannot be taken directly as a measure of  $Z_{\text{eff}}$  which must be finite for conductive systems. In these cases, electrons are only ‘‘nearly-free’’ rather than ‘‘truly-free’’ [67]. A finite scattering time must be taken into account when determining  $Z_{\text{eff}}$  from  $\bar{Z}^*(\omega)$ . As we will see, this can be done utilizing the low, but nonzero, frequency information available from nonadiabatic dynamics.

At finite frequency, the generalized DCS sum rule is written as,

$$\frac{1}{N_a} \sum_a Z_a^*(\omega) \equiv \bar{Z}^*(\omega) = i \frac{\omega}{n_a} \sigma(\omega) \equiv \bar{Z}_{\text{CD}}^*(\omega), \quad (3)$$

which can be understood as an equivalence of the electronic response under changing reference frames [61]. Here  $N_a$  is the number of atoms and  $n_a$  is the atomic number density. We define  $\bar{Z}_{\text{CD}}^*(\omega)$  as a conductivity-derived average

(CDA-) NBEC. This is simply a consequence of the conservation of momentum [68, 69]; the time-derivative of the total canonical electron momentum must oppose the total change in the atomic forces minus the contribution due to the bare ion interacting with the electric field,

$$\sum_a \delta \mathbf{F}^a(t)|_{\mathbf{R}^a(t)=\mathbf{R}^a(0)} - Z_a \mathbf{E}(t) = -\Omega \frac{d}{dt} \mathbf{J}(t). \quad (4)$$

In this fixed-ion limit, we assert that the momentum transferred to a particular atom or group of atoms (*e.g.*, atoms of the same element) can be used to define a unique group ( $G$ ) conductivity,

$$\sum_{a \in G} \frac{-i}{\Omega \omega} Z_a^*(\omega) \equiv \sigma^G(\omega), \quad (5)$$

$$\sum_G \sigma^G(\omega) \equiv \sigma^{\text{FD}}(\omega) = \sigma(\omega). \quad (6)$$

When summed over all groups the force-derived conductivity ( $\sigma^{\text{FD}}$ ) is equivalent to the conductivity from the generalized DCS sum rule in Eq. (3). This transformation gives clear meaning to the NBEC at all frequencies, allowing for the extraction of atomistic details of the electron transport.

We calculate the NBEC and conductivity by simultaneously obtaining the time-dependent change in the atomic forces and current density in response to an instantaneous macroscopic external electric field pulse along the  $x$ -direction,  $E_x(t) = \delta(t)E_{0,x}$ . In this letter, we focus on isotropic systems; therefore, the NBEC and conductivity tensors are diagonal, evaluated as,

$$Z_{xx}^*(\omega) + Z_a = \int dt e^{i\omega t - \frac{1}{4}\gamma^2 t^2} \Theta(t) \frac{F_x^a(t) - F_x^a(0)}{E_{0,x}}, \quad (7)$$

$$\sigma_{xx}(\omega) = \int dt e^{i\omega t - \frac{1}{4}\gamma^2 t^2} \Theta(t) \frac{J_x(t)}{E_{0,x}}. \quad (8)$$

While this approach to probe the linear-response conductivity has been previously reported [52, 70–72], the NBEC tensors have never been investigated in the WDM-HDP regime.

The Time-Dependent Kohn-Sham (TD-KS-DFT) approach used to calculate  $\mathbf{F}^a(t)$  and  $\mathbf{J}(t)$  is outlined in Supplemental Material Sec. S1 [52, 73–80]. To date only a single study has employed TD-KS-DFT to compute NBEC, relying on the current response to an instantaneous atomic displacement in crystalline systems [63]. Formally equivalent to Eq. (7), this approach lacks computational efficiency for multi-atom (disordered) systems that do not benefit from an expansive Brillouin zone sampling, see Supplemental Material. Our methodology allows for the simultaneous computation of  $\sigma$  and  $Z_a^*(\omega)$  for all atoms in a (disordered) system from a single TDDFT simulation. Without loss of information, from Eqs. (3) and (5), we consider and compare only the real-parts of  $\sigma(\omega)$ ,  $\sigma^{FD}(\omega)$ ,  $\bar{Z}^*(\omega)$  and  $\bar{Z}_{CD}^*(\omega)$ , *vide infra*.

Figure 1(a) shows the time-dependent current density ( $\mathbf{J}$ ), and atomic forces ( $\mathbf{F}$ ) in response to an instantaneous electric field pulse applied at  $t = 0$  for the cases of room-temperature fcc aluminium ( $k_B T = 0.025$  eV), and warm dense disordered aluminium ( $k_B T = 1.0$  eV). A Drude weight of 2.04 (Eq. (2)) is extracted for fcc Al in good agreement with previous results [63], see Supplemental Material. From Eq. (4),  $\frac{1}{n_a} \frac{\partial \mathbf{J}}{\partial t}$  is shown to be directly proportional to the average force; interestingly, unlike the fcc case  $\mathbf{J}(t)$  in WDM decays to zero due to disorder.

In Fig. 1 (b) the conductivity calculated from the current density ( $\sigma(\omega)$ ) is compared with the conductivity derived from the Drude weight ( $\sigma^G(\omega)$ , Eq. (5) used in conjunction with Eq. (2) for fcc Al. The Drude contribution is added as a Lorentzian centered at  $\omega = 0$  with a tenth of the artificial broadening (*vide infra*, Supplemental Material S2). Similarly, the inset of Fig. 1(b) shows an agreement between  $\bar{Z}^*(\omega)$  and  $\bar{Z}_{CD}^*(\omega)$ , Eq. (3). Finally, Fig. 1 (c) displays  $\bar{Z}^*(\omega)$  computed for a range of electronic temperatures in the fcc Al structure along with disordered phase Al at  $k_B T = 1.0$  eV. The electron transport properties in Al are largely unaffected by the increased electronic temperatures; the Drude weight remains  $\sim 2$  for up to  $k_B T = 5$  eV. Going from perfectly crystalline (blue dotted) to disordered (green dashed) eliminates the Drude weight contribution and  $\bar{Z}^*$  approaches 0 as  $\omega \rightarrow 0$ . This illustrates that  $Z_{\text{eff}}$ , which should be finite, and  $\bar{Z}^*(\omega \rightarrow 0)$  are inherently different quantities in WDM systems.

We now propose the extraction of the average  $Z_{\text{eff}}^G$  from  $\bar{Z}_G^*(\omega)$  in warm dense matter. As was used for the group conductivity,  $G$  indexes a given group of ions. We follow a typical approach of fitting the conductivity to the Drude-Smith model [81]. However, we also need to account for static charge transfer between groups,  $\Delta Z_{CT}^G \equiv \bar{Z}_G^*(0)$ . For group conductivity, the f-sum rule is now modified to include both the average bare-ion charge of the group,

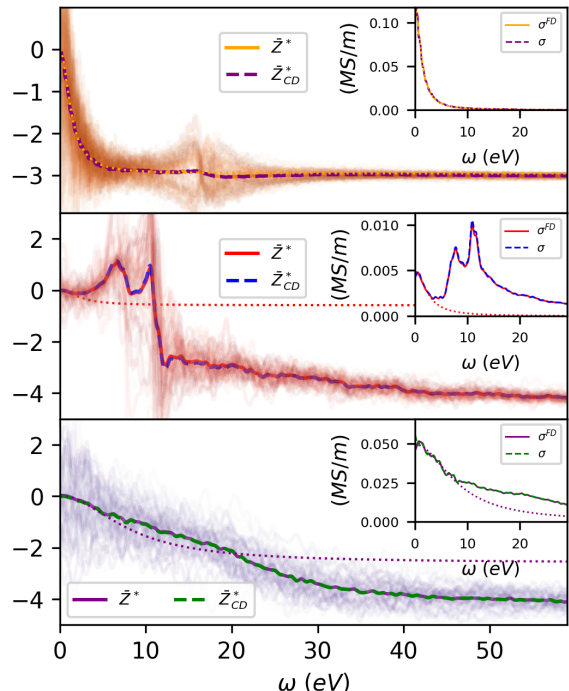


FIG. 2. The top panel shows the NBEC (inset- conductivity) for WDM disordered Al at  $k_B T = 1.0$  eV, while the middle and lower panels show low-density ( $0.5 \text{ g/cm}^3$ ) and solid-density ( $3.5 \text{ g/cm}^3$ ) warm dense carbon systems at  $k_B T = 5.0$  eV.

$Z_G$ , and  $\Delta Z_{CT}^G$ ,

$$\frac{2}{\pi} \int_0^\infty d\omega \sigma^G(\omega) = (Z_G + \Delta Z_{CT}^G) n_G, \quad (9)$$

where  $n_G$  is the number density of ions in group  $G$ . This follows from a straightforward application of the Kramers-Kronig relations to the force response. We thus modify the Drude-Smith model to account for charge transfer:

$$\sigma_{DS}(\tilde{Z}, \tilde{\tau}, n, c, \omega) = \frac{\tilde{Z} n \tilde{\tau}}{1 - i\omega \tilde{\tau}} \left[ 1 + \frac{c}{1 - i\omega \tilde{\tau}} \right],$$

$$\sigma_{DS}^G(\omega) \equiv \Re\{\sigma_{DS}(Z_{\text{eff}}^G + \Delta Z_{CT}^G, \tau_G, n_G, c_G; \omega)\},$$

$$\bar{Z}_{G,DS}^*(\omega) \equiv -\Im\{\omega \sigma_{DS}(\dots; \omega)\} + \Delta Z_{CT}^G. \quad (10)$$

Here  $\tau_G$  is the scattering time for the group,  $c_G$  is a parameter that suppresses the low-frequency contribution due to back-scattering [81]. If  $G$  includes all atoms of the system then  $\Delta Z_{CT} = 0$ . Drude-like behavior is inherently classical and emerges from quantum systems only when considering many ions. We identify that this approach is not applicable when  $G$  includes too few atoms. Therefore working in the large system size limit for mixed systems, we fit the conductivity for  $G$  comprising all atoms of a given elemental species.

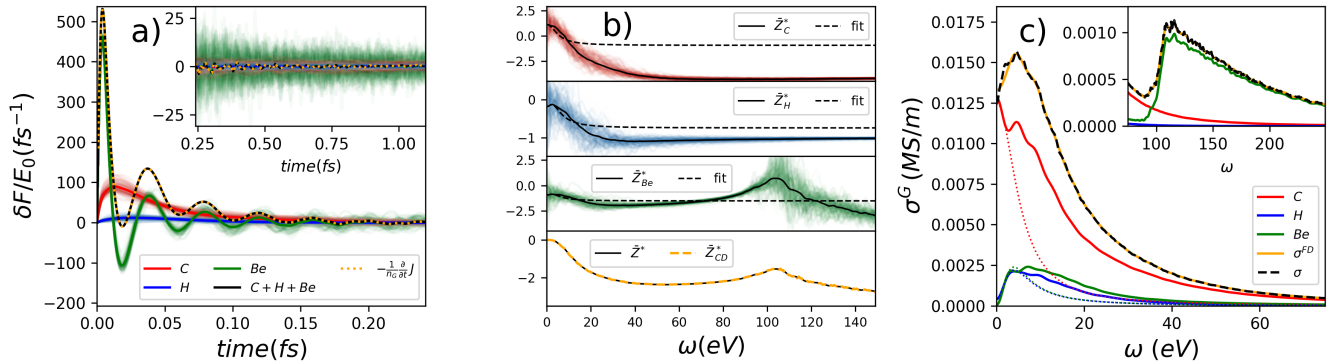


FIG. 3. Carbon Hydrogen Beryllium mixture,  $1.37 \text{ g/cm}^3$ ,  $k_B T = 5 \text{ eV}$ . a) The time-dependent individual and element average forces,  $F_x(t) - F_x(0)$ , the sum of the averages (black), and the  $3\times$  the scaled time-derivative of the current per atom (orange). b) atomic NBEC for different elements with average and Drude-Smith fit, bottom-average of all NBEC (black) and CDA-NBEC (orange). c) The total FD conductivity, along with the components from each element. The inset of a (resp. c) extends the time (resp. frequency) domain.

In Fig. 2 we show the average NBEC spectrum,  $\bar{Z}^*(\omega)$  (solid and dashed lines), along with individual atom contributions (gradient-shaded), and (insets)  $\sigma^G(\omega)$  for WDM systems. These average force-derived quantities are equivalent to their counterparts calculated from the current density, see Supplemental Material S3. While  $\bar{Z}^*(\omega)$  for Al is an essentially featureless-dissipative spectrum; the individual  $Z^*(\omega)$  show transition peaks between  $\hbar\omega = 10$  to  $20 \text{ eV}$ , which average to zero. These are the valence – continuum transitions, as only the  $3s^2 3p^1$  electrons are non-frozen (as part of the defined pseudopotential), with a very shallow Cooper minimum [82]. More prominent non-Drude transitions have been seen for  $\hbar\omega > 20 \text{ eV}$  from simulations including explicit  $2s^2 2p^6$  electrons [83]. Here,  $\sigma(\omega)$  or  $\sigma^{FD}(\omega)$  is fit to a Drude model yielding  $Z_{\text{eff}} = 2.9$  and  $\tau = 0.47 \text{ fs}$ . To make contact with the plasma physics models, we compare with the average-atom DFT code *Tartarus* [84] which furnishes two definitions of  $Z_{\text{eff}}$ ,  $Z_{\text{eff}}^{AA,1} = 2.0$  from the population of KS states with non-negative energy, and  $Z_{\text{eff}}^{AA,2} = 3.0$  from the population of KS states similar to the free-electron states [85].

The low-density ( $0.5 \text{ g/cm}^3$ ) carbon displays clear “bound-free” transitions, making fitting the NBEC spectrum to a Drude model a difficult task. The NBEC spectrum is composed of overlapping “dispersive” line-shapes and the high frequency asymptotic limit approaches the bare (minus frozen) ion charge of  $\sim -4$ . By transforming to the group conductivity (Eq. 5, insets), the peaks become “absorptive” and separate. Thus we fit the low-frequency portion of the group conductivity to the Drude model and extract a  $Z_{\text{eff}} = 0.58$  and  $\tau = 0.22 \text{ fs}$ ; compared to *Tartarus* which produces  $Z_{\text{eff}}^{AA,1} = 0.59$  and  $Z_{\text{eff}}^{AA,2} = 0.74$ . On the other hand, solid density carbon has a nearly featureless Drude-like conductivity and NBEC spectrum. Looking at  $\bar{Z}^*(\omega)$ , one may expect that the system characteristics follow a Drude behavior over

a large frequency range, yielding  $Z_{\text{eff}} \sim 4$ . However, the  $\sigma^G(\omega)$  reveals a distinct shoulder starting at  $\hbar\omega \sim 10 \text{ eV}$ . Therefore constraining the fit to low frequencies, we obtain a  $Z_{\text{eff}} = 2.8$  and  $\tau = 0.075 \text{ fs}$ ; *Tartarus* produces  $Z_{\text{eff}}^{AA,1} = 3.45$  and  $Z_{\text{eff}}^{AA,2} = 1.47$ . We must emphasize at this point that our formalism of nonadiabatic electron dynamics gives us access to scattering (relaxation) times which cannot be generated using static perturbation theory– based calculation. The distribution of  $Z^*(\omega)$  is significantly larger for the high-density carbon compared to the low-density, as evidenced by the purple and red gradient-shaded lines respectively, in Fig. 2. In all cases the Drude-Smith fits, based on fitting the group conductivity’s, are plotted alongside the calculated results for both  $\bar{Z}^*(\omega)$  and  $\sigma^{FD}(\omega)$ .

As a final example, we present a single warm dense mixture of equal parts hydrogen, beryllium and carbon, elements integral to inertial confinement fusion ablaters and recent experiments [86, 87], at a density of  $1.37 \text{ g/cm}^3$  and  $k_B T = 5 \text{ eV}$ . This system comprises a large simulation box with 128 atoms of each element and high temperature with a relatively low density; physical conditions that challenge the deterministic KS approach [73, 74]. Hence we employ a recently developed mixed stochastic-deterministic TDDFT to converge the simulation [52, 73]. The force response of each ion (inset) and their element-wise and all-ion averages are shown in Fig. 3(a). As expected, the average force for all ions nearly exactly opposes the time-derivative of the current density per atom (from Eq. (4)). Due to the explicit treatment of Be– $1s$  electrons in the pseudopotential, the Be response features long-lived oscillations which quickly average to zero, but individually persist. In Fig. 3(b), the NBEC’s for ions of each species are shown along with  $\bar{Z}(\omega)$  and  $\bar{Z}^{CD}(\omega)$ . Figure 3 (c) shows the group conductivity for each element type, the sum of the contributions,  $\sigma^{FD}$ , and the conductivity  $\sigma$  are shown.

The peak in the conductivity starting at  $\hbar\omega \sim 100$  eV is solely attributed to Be, though it overlaps with the tail of the carbon contribution. The Drude-Smith fits to low frequency segments of each  $\sigma^G(\omega)$  yield  $\bar{Z}_{\text{eff}}^C = 0.94$ ,  $\bar{Z}_{\text{eff}}^H = 1.00$ , and  $\bar{Z}_{\text{eff}}^{Be} = 2.23$  along with  $\tau_C = 0.12$  fs,  $\tau_H = 0.16$  fs, and  $\tau_{Be} = 0.17$  fs, and  $c_C = 0.0$ ,  $c_H = -0.91$ , and  $c_{Be} = -0.99$ . The NBEC calculations indicate charge transfer occurring between the groups, with  $\Delta Z_{CT}^C = +1.11$ ,  $\Delta Z_{CT}^H = -0.18$ , and  $\Delta Z_{CT}^{Be} = -0.94$ , which follows from the electronegativity of each species.

We present a new formalism for a more efficient calculation of the  $Z_a^*(\omega)$  for all atoms in a unit cell from TDDFT simulations. *Ab initio* calculations of  $Z_a^*(\omega)$  could help develop a more complete understanding of the initial nonequilibrium ion-velocity distribution resulting from pulsed laser excitations in the extreme ultraviolet and soft X-ray regimes. Transforming  $Z_a^*(\omega)$  to the force-derived  $\sigma^{FD}(\omega)$  provides a logical interpretation of the high frequency and imaginary parts of  $Z_a^*(\omega)$ . Our simulations also provide the first numerical validation of the DCS sum rule beyond the static limit. In the warm dense matter regime described here, averaging  $Z_a^*(\omega)$  over a sufficiently large number of atoms allows determination of  $Z_{\text{eff}}^G$  for a subgroup of (or all) atoms. These results tend to fall between the disparate definitions from an average atom code [42]. When applied to the mixed C:H:Be system, we see charge transfer between the element groups,

which unveils a new complexity to the electronic structure of warm dense matter mixtures. This could play a significant role in the mixing of equation-of-state or conductivity tables and model development. Moreover, during the generation of mixed conductivity spectra, the weighted contributions of different species could be compared against the group conductivities,  $\sigma^G(\omega)$ , generated by our proposed approach.

## ACKNOWLEDGMENTS

This work was supported by the U.S. Department of Energy through the Los Alamos National Laboratory (LANL). Research presented in this article was supported by the Laboratory Directed Research and Development program, projects number 20230322ER and 20230323ER, and the Institute for Material Science, projects number 20248109CT-IMS, of LANL. We acknowledge the support of the Center for Nonlinear Studies (CNLS). This research used computing resources provided by the LANL Institutional Computing and Advanced Scientific Computing programs. Los Alamos National Laboratory is operated by Triad National Security, LLC, for the National Nuclear Security Administration of U.S. Department of Energy (Contract No. 89233218CNA000001).

- 
- [1] M. Bonitz, T. Dornheim, Z. A. Moldabekov, S. Zhang, P. Hamann, H. Kählert, A. Filinov, *et al.*, *Ab initio* simulation of warm dense matter, *Physics of Plasmas* **27**, 042710 (2020).
- [2] T. Dornheim, Z. A. Moldabekov, K. Ramakrishna, P. Toliás, A. D. Baczewski, D. Kraus, T. R. Preston, *et al.*, Electronic density response of warm dense matter, *Physics of Plasmas* **30**, 032705 (2023).
- [3] K. Falk, Experimental methods for warm dense matter research, *High Power Laser Science and Engineering* **6**, e59 (2018).
- [4] W. Lorenzen, A. Becker, and R. Redmer, Progress in warm dense matter and planetary physics, in *Frontiers and Challenges in Warm Dense Matter*, edited by F. Graziani, M. P. Desjarlais, R. Redmer, and S. B. Trickey (Springer International Publishing, Cham, 2014) pp. 203–234.
- [5] V. B. Prakapenka, N. Holtgrewe, S. S. Lobanov, and A. F. Goncharov, Structure and properties of two superionic ice phases, *Nature Physics* **17**, 1233 (2021).
- [6] D. e. a. Ehrenreich, Nightside condensation of iron in an ultrahot giant exoplanet, *Nature* **580**, 597 (2020).
- [7] H. e. a. Abu-Shawareb (The Indirect Drive ICF Collaboration), Achievement of Target Gain Larger than Unity in an Inertial Fusion Experiment, *Phys. Rev. Lett.* **132**, 065102 (2024).
- [8] M. S. Murillo, J. Weisheit, S. B. Hansen, and M. W. C. Dharma-Wardana, Partial ionization in dense plasmas: Comparisons among average-atom density functional models, *Phys. Rev. E* **87**, 063113 (2013).
- [9] P. Grabowski, S. Hansen, M. Murillo, L. Stanton, F. Graziani, A. Zylstra, S. Baalrud, *et al.*, Review of the first charged-particle transport coefficient comparison workshop, *High Energy Density Physics* **37**, 100905 (2020).
- [10] L. J. Stanek, A. Kononov, S. B. Hansen, B. M. Haines, S. X. Hu, P. F. Knapp, M. S. Murillo, *et al.*, Review of the second charged-particle transport coefficient code comparison workshop, *Physics of Plasmas* **31**, 052104 (2024).
- [11] B. M. Haines, Charged particle transport coefficient challenges in high energy density plasmas, *Physics of Plasmas* **31**, 050501 (2024).
- [12] R. S. Cohen, L. Spitzer, and P. M. Routly, The Electrical Conductivity of an Ionized Gas, *Phys. Rev.* **80**, 230 (1950).
- [13] Y. T. Lee and R. M. More, An electron conductivity model for dense plasmas, *The Physics of Fluids* **27**, 1273 (1984).
- [14] D. Munro and S. Weber, Electron thermal conduction in LASNEX [10.2172/95342](https://doi.org/10.2172/95342) (1994).
- [15] M. Desjarlais, Practical Improvements to the Lee-More Conductivity Near the Metal-Insulator Transition, *Contributions to Plasma Physics* **41**, 267 (2001).
- [16] F. Perrot and M. W. C. Dharma-Wardana, Electrical resistivity of hot dense plasmas, *Phys. Rev. A* **36**, 238 (1987).
- [17] L. Spitzer and R. Härm, Transport Phenomena in a Completely Ionized Gas, *Phys. Rev.* **89**, 977 (1953).

- [18] E. Nardi, Z. Zinamon, D. Riley, and N. C. Woolsey, X-ray scattering as a dense plasma diagnostic, *Phys. Rev. E* **57**, 4693 (1998).
- [19] B. Lihua, Z. Jiyan, Z. Xiaoding, Z. Yang, and D. Yongkun, Observations of non-collective x-ray scattering in warm dense carbon plasma, *Physics of Plasmas* **19**, 122709 (2012).
- [20] D. Kraus, D. A. Chapman, A. L. Kritcher, R. A. Baggott, B. Bachmann, G. W. Collins, S. H. Glenzer, *et al.*, X-ray scattering measurements on imploding CH spheres at the National Ignition Facility, *Phys. Rev. E* **94**, 011202 (2016).
- [21] T. Döppner, M. Bethkenhagen, D. Kraus, P. Neumayer, D. A. Chapman, B. Bachmann, R. A. Baggott, *et al.*, Observing the onset of pressure-driven K-shell delocalization, *Nature* **618**, 270 (2023).
- [22] J. Ren, Z. Deng, W. Qi, B. Chen, B. Ma, X. Wang, S. Yin, *et al.*, Observation of a high degree of stopping for laser-accelerated intense proton beams in dense ionized matter, *Nature Communications* **11**, 5157 (2020).
- [23] S. Malko, W. Cayzac, V. Ospina-Bohórquez, K. Bhutwala, M. Bailly-Grandvaux, C. McGuffey, R. Fedosejevs, *et al.*, Proton stopping measurements at low velocity in warm dense carbon, *Nature Communications* **13**, 2893 (2022).
- [24] C.-K. Li and R. D. Petrasso, Charged-particle stopping powers in inertial confinement fusion plasmas, *Phys. Rev. Lett.* **70**, 3059 (1993).
- [25] G. Maynard and C. Deutsch, Energy loss and straggling of ions with any velocity in dense plasmas at any temperature, *Phys. Rev. A* **26**, 665 (1982).
- [26] D. Gericke, M. Schlages, and W. Kraeft, Stopping power of a quantum plasma — T-matrix approximation and dynamical screening, *Physics Letters A* **222**, 241 (1996).
- [27] L. S. Brown, D. L. Preston, and R. L. Singleton Jr., Charged particle motion in a highly ionized plasma, *Physics Reports* **410**, 237 (2005).
- [28] C. F. Clauser and N. R. Arista, Stopping power of dense plasmas: The collisional method and limitations of the dielectric formalism, *Phys. Rev. E* **97**, 023202 (2018).
- [29] D. Casas, M. D. Barriga-Carrasco, and J. Rubio, Evaluation of slowing down of proton and deuteron beams in CH<sub>2</sub>, LiH, and Al partially ionized plasmas, *Phys. Rev. E* **88**, 033102 (2013).
- [30] J. R. Stallcop and K. W. Billman, Analytical formulae for the inverse bremsstrahlung absorption coefficient, *Plasma Physics* **16**, 1187 (1974).
- [31] D. Turnbull, J. Katz, M. Sherlock, L. Divol, N. R. Shaffer, D. J. Strozzi, A. Colaitis, D. H. Edgell, R. K. Follert, K. R. McMillen, P. Michel, A. L. Milder, and D. H. Froula, Inverse Bremsstrahlung Absorption, *Phys. Rev. Lett.* **130**, 145103 (2023).
- [32] D. Turnbull, J. Katz, M. Sherlock, A. L. Milder, M. S. Cho, L. Divol, N. R. Shaffer, *et al.*, Reconciling calculations and measurements of inverse bremsstrahlung absorption, *Physics of Plasmas* **31**, 063304 (2024).
- [33] W. L. Slattery, G. D. Doolen, and H. E. DeWitt, Improved equation of state for the classical one-component plasma, *Phys. Rev. A* **21**, 2087 (1980).
- [34] F. J. Rogers, Ionization equilibrium and equation of state in strongly coupled plasmas, *Physics of Plasmas* **7**, 51 (2000).
- [35] J. Clérouin, P. Arnault, C. Ticknor, J. D. Kress, and L. A. Collins, Unified Concept of Effective One Component Plasma for Hot Dense Plasmas, *Phys. Rev. Lett.* **116**, 115003 (2016).
- [36] C. Ticknor, J. D. Kress, L. A. Collins, J. Clérouin, P. Arnault, and A. Decoster, Transport properties of an asymmetric mixture in the dense plasma regime, *Phys. Rev. E* **93**, 063208 (2016).
- [37] A. J. White, L. A. Collins, J. D. Kress, C. Ticknor, J. Clérouin, P. Arnault, and N. Desbiens, Correlation and transport properties for mixtures at constant pressure and temperature, *Phys. Rev. E* **95**, 063202 (2017).
- [38] J. P. Hansen, G. M. Torrie, and P. Vieillefosse, Statistical mechanics of dense ionized matter. VII. Equation of state and phase separation of ionic mixtures in a uniform background, *Phys. Rev. A* **16**, 2153 (1977).
- [39] S. Bastea, Viscosity and mutual diffusion in strongly asymmetric binary ionic mixtures, *Phys. Rev. E* **71**, 056405 (2005).
- [40] E. M. Epperlein and M. G. Haines, Plasma transport coefficients in a magnetic field by direct numerical solution of the Fokker-Planck equation, *The Physics of Fluids* **29**, 1029 (1986).
- [41] J. Clérouin, P. Arnault, B.-J. Gréa, S. Guisset, M. Vandenboomgaerde, A. J. White, L. A. Collins, J. D. Kress, and C. Ticknor, Static and dynamic properties of multi-ionic plasma mixtures, *Phys. Rev. E* **101**, 033207 (2020).
- [42] C. Starrett, N. Shaffer, D. Saumon, R. Perriot, T. Nelson, L. Collins, and C. Ticknor, Model for the electrical conductivity in dense plasma mixtures, *High Energy Density Physics* **36**, 100752 (2020).
- [43] A. J. White, G. T. Craven, V. Sharma, and L. A. Collins, Optical and transport properties of plasma mixtures from ab initio molecular dynamics, *Physics of Plasmas* **31**, 042706 (2024).
- [44] R. P. Drake, Properties of high-energy-density plasmas, in *High-Energy-Density Physics: Foundation of Inertial Fusion and Experimental Astrophysics* (Springer International Publishing, Cham, 2018) pp. 51–114.
- [45] S. X. Hu, L. A. Collins, V. N. Goncharov, J. D. Kress, R. L. McCrory, and S. Skupsky, First-principles investigations on ionization and thermal conductivity of polystyrene for inertial confinement fusion applications, *Physics of Plasmas* **23**, 042704 (2016).
- [46] R. Ying and G. Kalman, Thomas-Fermi model for dense plasmas, *Phys. Rev. A* **40**, 3927 (1989).
- [47] R. S. Mulliken, Electronic Population Analysis on LCAO-MO Molecular Wave Functions. I, *The Journal of Chemical Physics* **23**, 1833 (1955).
- [48] R. F. W. Bader, Atoms in molecules, *Accounts of Chemical Research* **18**, 9 (1985).
- [49] F. L. Hirshfeld, Bonded-atom fragments for describing molecular charge densities, *Theoretica chimica acta* **44**, 129 (1977).
- [50] K. B. Wiberg and P. R. Rablen, Atomic Charges, *The Journal of Organic Chemistry* **83**, 15463 (2018).
- [51] C. Ertural, S. Steinberg, and R. Dronskowski, Development of a robust tool to extract mulliken and löwdin charges from plane waves and its application to solid-state materials, *RSC Adv.* **9**, 29821 (2019).
- [52] A. J. White, L. A. Collins, K. Nichols, and S. X. Hu, Mixed stochastic-deterministic time-dependent density functional theory: application to stopping power of warm dense carbon, *Journal of Physics: Condensed Matter* **34**, 174001 (2022).
- [53] M. Bethkenhagen, B. B. L. Witte, M. Schörner,

- G. Röpke, T. Döppner, D. Kraus, S. H. Glenzer, *et al.*, Carbon ionization at gigabar pressures: An ab initio perspective on astrophysical high-density plasmas, *Phys. Rev. Res.* **2**, 023260 (2020).
- [54] S. X. Hu, Continuum Lowering and Fermi-Surface Rising in Strongly Coupled and Degenerate Plasmas, *Phys. Rev. Lett.* **119**, 065001 (2017).
- [55] K. P. Driver, F. Soubiran, and B. Militzer, Path integral Monte Carlo simulations of warm dense aluminum, *Phys. Rev. E* **97**, 063207 (2018).
- [56] P. Ghosez, J.-P. Michenaud, and X. Gonze, Dynamical atomic charges: The case of  $\text{ABO}_3$  compounds, *Phys. Rev. B* **58**, 6224 (1998).
- [57] M. Born and K. Huang, *Dynamical Theory of Crystal Lattices* (1998).
- [58] S. Baroni, S. de Gironcoli, A. Dal Corso, and P. Giannozzi, Phonons and related crystal properties from density-functional perturbation theory, *Rev. Mod. Phys.* **73**, 515 (2001).
- [59] P. T. Mahon and J. E. Sipe, Electric polarization and magnetization in metals, *SciPost Phys.* **14**, 058 (2023).
- [60] R. Resta and D. Vanderbilt, Theory of polarization: A modern approach, in *Physics of Ferroelectrics: A Modern Perspective* (Springer Berlin Heidelberg, Berlin, Heidelberg, 2007) pp. 31–68.
- [61] C. E. Dreyer, S. Coh, and M. Stengel, Nonadiabatic Born Effective Charges in Metals and the Drude Weight, *Phys. Rev. Lett.* **128**, 095901 (2022).
- [62] E. Runge and E. K. U. Gross, Density-Functional Theory for Time-Dependent Systems, *Phys. Rev. Lett.* **52**, 997 (1984).
- [63] C.-Y. Wang, S. Sharma, E. K. U. Gross, and J. K. Dewhurst, Dynamical Born effective charges, *Phys. Rev. B* **106**, L180303 (2022).
- [64] R. M. Pick, M. H. Cohen, and R. M. Martin, Microscopic Theory of Force Constants in the Adiabatic Approximation, *Phys. Rev. B* **1**, 910 (1970).
- [65] G. Bellomia and R. Resta, Drude weight in systems with open boundary conditions, *Phys. Rev. B* **102**, 205123 (2020).
- [66] R. Resta, Drude weight and superconducting weight, *Journal of Physics: Condensed Matter* **30**, 414001 (2018).
- [67] R. More, Pressure Ionization, Resonances, and the Continuity of Bound and Free States (Academic Press, 1985) pp. 305–356.
- [68] J. Daligault and J. Simoni, Theory of the electron-ion temperature relaxation rate spanning the hot solid metals and plasma phases, *Phys. Rev. E* **100**, 043201 (2019).
- [69] G. Marchese, F. Macheda, L. Binci, M. Calandra, P. Barone, and F. Mauri, Born effective charges and vibrational spectra in superconducting and bad conducting metals, *Nature Physics* **20**, 88 (2024).
- [70] Andrade, Xavier, Hamel, Sébastien, and Correa, Alfredo A., Negative differential conductivity in liquid aluminum from real-time quantum simulations, *Eur. Phys. J. B* **91**, 229 (2018).
- [71] A. Kononov, C.-W. Lee, T. P. dos Santos, B. Robinson, Y. Yao, Y. Yao, X. Andrade, A. D. Baczewski, E. Constantinescu, A. A. Correa, Y. Kanai, N. Modine, and A. Schleife, Electron dynamics in extended systems within real-time time-dependent density-functional theory, *MRS Communications* **12**, 1002 (2022).
- [72] A. Kononov, A. J. White, K. A. Nichols, S. X. Hu, and A. D. Baczewski, Reproducibility of real-time time-dependent density functional theory calculations of electronic stopping power in warm dense matter, *Physics of Plasmas* **31**, 043904 (2024).
- [73] A. J. White and L. A. Collins, Fast and Universal Kohn-Sham Density Functional Theory Algorithm for Warm Dense Matter to Hot Dense Plasma, *Phys. Rev. Lett.* **125**, 055002 (2020).
- [74] V. Sharma, L. A. Collins, and A. J. White, Stochastic and mixed density functional theory within the projector augmented wave formalism for simulation of warm dense matter, *Phys. Rev. E* **108**, L023201 (2023).
- [75] N. D. Mermin, Thermal Properties of the Inhomogeneous Electron Gas, *Phys. Rev.* **137**, A1441 (1965).
- [76] T. J. Park and J. C. Light, Unitary quantum time evolution by iterative Lanczos reduction, *The Journal of Chemical Physics* **85**, 5870 (1986).
- [77] S. Goedecker, M. Teter, and J. Hutter, Separable dual-space Gaussian pseudopotentials, *Phys. Rev. B* **54**, 1703 (1996).
- [78] D. R. Hamann, Optimized norm-conserving Vanderbilt pseudopotentials, *Phys. Rev. B* **88**, 085117 (2013).
- [79] M. van Setten, M. Giantomassi, E. Bousquet, M. Verstraete, D. Hamann, X. Gonze, and G.-M. Rignanese, The PseudoDojo: Training and grading a 85 element optimized norm-conserving pseudopotential table, *Computer Physics Communications* **226**, 39 (2018).
- [80] H. J. Monkhorst and J. D. Pack, Special points for Brillouin-zone integrations, *Phys. Rev. B* **13**, 5188 (1976).
- [81] T. L. Cocker, D. Baillie, M. Buruma, L. V. Titova, R. D. Sydora, F. Marsiglio, and F. A. Hegmann, Microscopic origin of the Drude-Smith model, *Phys. Rev. B* **96**, 205439 (2017).
- [82] J. W. Cooper, Photoionization from Outer Atomic Subshells. A Model Study, *Phys. Rev.* **128**, 681 (1962).
- [83] B. B. L. Witte, L. B. Fletcher, E. Galtier, E. Gamboa, H. J. Lee, U. Zastra, R. Redmer, S. H. Glenzer, and P. Sperling, Warm Dense Matter Demonstrating Non-Drude Conductivity from Observations of Nonlinear Plasmon Damping, *Phys. Rev. Lett.* **118**, 225001 (2017).
- [84] N. Gill and C. Starrett, Tartarus: A relativistic Green's function quantum average atom code, *High Energy Density Physics* **24**, 33 (2017).
- [85] C. Starrett, N. Gill, T. Sjoström, and C. Greeff, Wide ranging equation of state with Tartarus: A hybrid Green's function/orbital based average atom code, *Computer Physics Communications* **235**, 50 (2019).
- [86] O. A. Hurricane, P. K. Patel, R. Betti, D. H. Froula, S. P. Regan, S. A. Slutz, M. R. Gomez, and M. A. Sweeney, Physics principles of inertial confinement fusion and U.S. program overview, *Rev. Mod. Phys.* **95**, 025005 (2023).
- [87] S. Jiang, O. L. Landen, H. D. Whitley, S. Hamel, R. London, D. S. Clark, P. Sterne, S. B. Hansen, S. X. Hu, G. W. Collins, and Y. Ping, Thermal transport in warm dense matter revealed by refraction-enhanced x-ray radiography with a deep-neural-network analysis, *Communications Physics* **6**, 98 (2023).

Supplemental Material for

**Group Conductivity and Dynamical Born Effective Charges of Disordered Metals, Warm Dense Matter and Dense Plasma Mixtures**

Vidushi Sharma<sup>1,2,3</sup> and Alexander J. White<sup>1</sup>

<sup>1</sup>*Theoretical Division, Los Alamos National Laboratory, Los Alamos, NM 87545, USA*

<sup>2</sup>*Center for Nonlinear Studies (CNLS), Los Alamos National Laboratory, Los Alamos, NM 87545, USA*

<sup>3</sup>*Applied Materials and Sustainability Sciences, Princeton Plasma Physics Laboratory, Princeton, NJ 08540-6655, USA*

(Dated: August 30, 2024)

**S1. TIME-DEPENDENT KOHN-SHAM APPROACH TO LINEAR RESPONSE CONDUCTIVITY AND NONADIABATIC BORN EFFECTIVE CHARGE**

Since conductivity and NBEC are quantum mechanical observables with well-defined operators, they can be calculated using any time-dependent or excited-state electronic structure method. Here we calculate and analyze the NBEC and group conductivity for bulk systems using time-dependent Kohn-Sham density functional theory. We utilize atomic units such that the mass of electron,  $m_e$ , and the reduced Planck's constant  $\hbar$  are unity. Within linear response, the time-dependent NBEC tensor is defined as the response function of the negative of the atomic force vector with respect to the electric field vector,

$$d\mathbf{F}^a(t, \mathbf{q}) \equiv - \int \int dt' d\mathbf{q}' \hat{Z}_a^*(t, t', \mathbf{q}, \mathbf{q}') \cdot d\mathbf{E}(\mathbf{q}', t'), \quad (\text{S1})$$

while the conductivity tensor is defined by a similar equation with the negative of the force replaced by the current density,

$$d\mathbf{J}(t, \mathbf{q}) \equiv \int \int dt' d\mathbf{q}' \hat{\sigma}(t, t', \mathbf{q}, \mathbf{q}') \cdot d\mathbf{E}(\mathbf{q}', t'). \quad (\text{S2})$$

Here  $\mathbf{q}$  is the perturbation wavevector. If we consider a macroscopic instantaneous electric field pulse along the arbitrary x-direction  $dE_x(q', t') = E_0 \delta(q') \delta(t')$ , we can obtain the macroscopic NBEC / conductivity via

$$\hat{Z}_{a,y,x}^*(\omega) \equiv \mathcal{F}[\Theta(t) dF^{a,y}(t)/E_0](\omega), \quad (\text{S3})$$

$$\sigma_{y,x}^*(\omega) \equiv \mathcal{F}[\Theta(t) dJ^y(t)/E_0](\omega), \quad (\text{S4})$$

where  $\mathcal{F}[\dots]$  denotes the Fourier transform from the forward time  $t$  to angular-frequency  $\omega$ ; the Heaviside function,  $\Theta(t)$  is included to ensure causality.

To calculate the time-dependent forces and current from the adiabatic time dependent Kohn-Sham density functional theory (TD-KS-DFT) we solve the equation of motion for the KS Bloch orbitals:

$$\frac{i\partial}{\partial t} u_b^{\mathbf{k}}(\mathbf{r}, t) = \hat{H}_{KS}^{\mathbf{k}}(t) u_b^{\mathbf{k}}(t), \quad (\text{S5})$$

$$\hat{H}_{KS}^{\mathbf{k}}(t) = \frac{-1}{2} (\hat{\nabla} + i\mathbf{A}(t) + i\mathbf{k})^2 + V_{XC,H}(\mathbf{r}, \rho(t)) + V_{ei,LPP}(\mathbf{r}, \mathbf{R}) + \hat{V}_{ei,NLPP}^{\mathbf{k}}(\mathbf{R}). \quad (\text{S6})$$

Here the term adiabatic refers to the dependence of the exchange correlation (plus Hartree) potential,  $\hat{V}_{XC,H}$ , on only the instantaneous time-dependent density,  $\rho(t)$ ;  $\mathbf{r}$  is the real-space electron position vector while  $\mathbf{R}$  is the ion position vector,  $\mathbf{k}$  is the k-point associated with this Bloch orbital. When using pseudopotentials (PP), the electron-ion interaction has a local part,  $V_{ei,LPP}(\mathbf{r}, \mathbf{R})$ , and possibly a nonlocal part,  $\hat{V}_{ei,NLPP}^{\mathbf{k}}(\mathbf{R})$ . The time dependent density (density matrix) is given by:

$$\rho(\mathbf{r}, t) = \delta(\mathbf{r}, \mathbf{r}') \rho(\mathbf{r}, \mathbf{r}', t) = \delta(\mathbf{r}, \mathbf{r}') \sum_{\mathbf{k}, b} f(\varepsilon_b^{\mathbf{k}}, \mu, T) u_b^{\mathbf{k}}(\mathbf{r}, t) u_b^{*\mathbf{k}}(\mathbf{r}', t), \quad \text{where} \quad (\text{S7})$$

$$f(\varepsilon, \mu, T) := \frac{1}{1 + e^{(\varepsilon - \mu)/k_B T}}. \quad (\text{S8})$$



In the Mermin extension of TD-KS-DFT the finite electron temperature [75],  $T$ , enters only through the Fermi-Dirac occupations, which depend on the equilibrium Mermin-DFT eigenenergies,  $\varepsilon$ , and the electron chemical potential,  $\mu$ . For mixed stochastic-deterministic KS-DFT, the density matrix contains also the complementary stochastic vectors, which take a similar low-rank form to Eq. S7, and it is propagated by the same TD approach as the deterministic orbitals [52, 73, 74].

For our instantaneous electric field pulse along  $x$ , the vector potential is a step function,  $\mathbf{A}(t) \equiv -\hat{e}_x E_0 \Theta(t)$ . Recall that  $\mathbf{E}(t) = -\frac{\partial}{\partial t} \mathbf{A}(t)$ . The electron momentum is thus instantaneously increased and relaxes due to disorder. From the Mermin DFT approach, the initial current density before the pulse is zero,  $J(t < 0) = 0$ .

The force is calculated using the energy-conserving Ehrenfest, expression:

$$F^{a,y}(f) = \int d\mathbf{r} \left[ \left\{ \frac{\partial}{\partial R_{a,y}} V_{ei,\text{LPP}}(\mathbf{r}, \mathbf{R}) \right\} \rho(\mathbf{r}, t) \right] + \sum_{b,\mathbf{k}} \int \int d\mathbf{r} d\mathbf{r}' f(\varepsilon_b^{\mathbf{k}}, \mu, T) u_b^{\mathbf{k}*}(\mathbf{r}', t) \left\{ \frac{\partial}{\partial R_{a,y}} V_{ei,\text{NLPP}}(\mathbf{r}, \mathbf{r}', \mathbf{R}) \right\} u_b^{\mathbf{k}}(\mathbf{r}, t). \quad (\text{S9})$$

The total electron current and can be decomposed into the diamagnetic part, a contribution coming directly from electron density  $\rho(r)$  and the vector potential and the paramagnetic part, coming from the time-dependent density matrix,  $\hat{\rho}(t)$ ,

$$\mathbf{J}(t) = \int d\mathbf{r} \mathbf{A}(r, t) \rho(r) + \text{Tr} [\{\hat{\mathbf{p}}\} \hat{\rho}(t)] , \quad (\text{S10})$$

where  $\mathbf{p} = (-i\nabla + \mathbf{k})$  is the canonical electron momentum. Non-local Hamiltonian terms, such as arising from pseudopotentials, add additional terms to the “full” momentum, as defined via  $\mathbf{p}' = i[\hat{H}_{KS}^{\mathbf{k}}, \mathbf{r}]$ . This “full” definition retains consistency of the dipole and the momentum operators, while the first fulfils the exact momentum conservation and thus the generalized Dreyer, Coh, and Stengel (DCS) rule as well as the f-sum rule [61, 66]. We employ the canonical momentum in the letter and note that differences are typically less than  $\sim 10$  percent.

For simplicity, we only discuss response parallel to the perturbation, dropping vector and tensor notation, and only concern ourselves with the macroscopic ( $q \rightarrow 0$ ) limit. We consider only isotropic systems in the letter and thus, do not investigate the off-diagonal elements of the NBEC or conductivity tensors.

## S2. CURRENT RESPONSE TO MACROSCOPIC ELECTRIC FIELD PULSE AND THE DRUDE WEIGHT

The conductivity can be separated into two parts, the regular and Drude contributions, [65, 66]

$$\sigma(\omega) = \frac{D}{\pi} \left\{ \frac{1}{2} \delta(\omega) + \frac{i}{\omega} \right\} + \sigma_{\text{reg}}(\omega) . \quad (\text{S11})$$

The Drude part,  $\propto D/\pi$ , and regular conductivity,  $\sigma_{\text{reg}}$ , are associated with intraband and interband transitions, respectively. Finite  $D$  implies the presence of free charge carriers, *i.e.*, a finite long-time current density  $\mathbf{J}(t \rightarrow \infty) \neq 0$  in response to an instantaneous macroscopic electric field pulse at  $t = 0$ . The electric field imparts momentum to all the electrons equally, but some electrons have high inertia and thus there is a finite current at long times, *i.e.*, times on the order of ion motion or phonon frequencies. Finite simulation time and system size necessitate a dampening of the current before the Fourier transformation, leading to a broadening of the conductivity peaks and a finite regular conductivity at  $\omega = 0$ . By causality, the imaginary part of the conductivity,  $\Im[\sigma(\omega)]$ , is an odd function, so the real part of the  $\Re[i\omega \sigma(\omega)]|_{\omega=0} = 0$ , therefore from

$$i\omega \hat{\sigma}(\omega) \equiv -\frac{\hat{D}}{\pi} + i\omega \hat{\sigma}_{\text{reg}}(\omega) , \quad \text{and} \quad (\text{S12})$$

$$i\omega \hat{\sigma}_{\text{reg}}(\omega) = \frac{\mathbf{J}(0^+)}{\mathbf{E}_0} + \frac{1}{\mathbf{E}_0} \mathcal{F} \left[ \Theta(t) e^{-\frac{1}{4}\gamma^2 t^2} \frac{\partial}{\partial t} \mathbf{J}(t, \mathbf{q} = 0) \right] (\omega) , \quad (\text{S13})$$

we can extract the Drude weight,  $\hat{D}/\pi = \Re[i\omega \hat{\sigma}_{\text{reg}}(\omega)]|_{\omega=0}$ , directly from the current in the presence of a broadened ( $\gamma > 0$ ) regular conductivity. To have the correct  $\omega \rightarrow \infty$  behavior in  $i\omega \hat{\sigma}(\omega)$ , the dampening term is included after taking the time-derivative. Since electrons cannot respond instantaneously to the pulse, the current at a time instant infinitesimally after the pulse is proportional to the electric field strength and the electron density,  $\mathbf{J}(0^+) = n_e \mathbf{E}_0$ , which implies,  $\int \frac{d\omega}{2\pi} \sigma(\omega) = \frac{n_e}{2}$ . [66] This is the well-known f-sum rule. More simply put, the Drude weight is proportional to the initial current density plus the (negative) change in the current density over a long time, *i.e.*, it is the *unrelaxed* part of the current density.

**S3. VALIDATION OF APPROACH AGAINST SYSTEMS SIMULATED IN “DYNAMICAL BORN EFFECTIVE CHARGES” BY C.-YU WANG, S. SHARMA, E. K. U. GROSS, AND J. K. DEWHURST [63]**

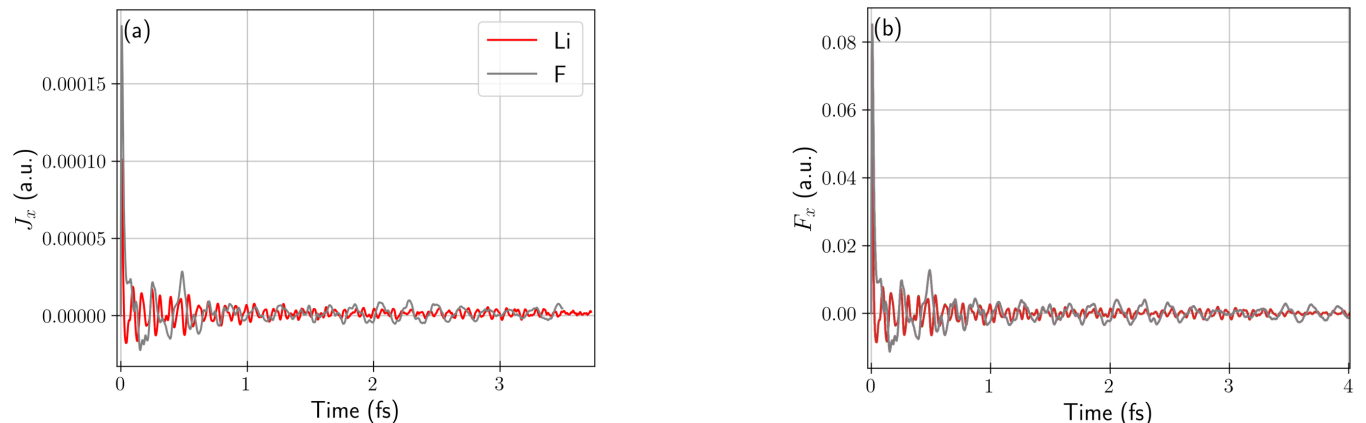


FIG. S1. LiF fcc crystal structure with an 8-atom unit cell and a  $[20 \times 20 \times 20]$  Monkhorst-pack  $k$ -grid: (a) Current density signal decay with time for an initial perturbation given by an atomic displacement  $\lambda(t = 0^-) : \delta r = 0.01$  a.u., in the  $x$ -direction. (b) Forces exerted on the atoms by the electronic density in response to an electric field pulse uniform in space in the long-wavelength limit  $\lambda(t = 0^-) : E_x = 0.01$  a.u.

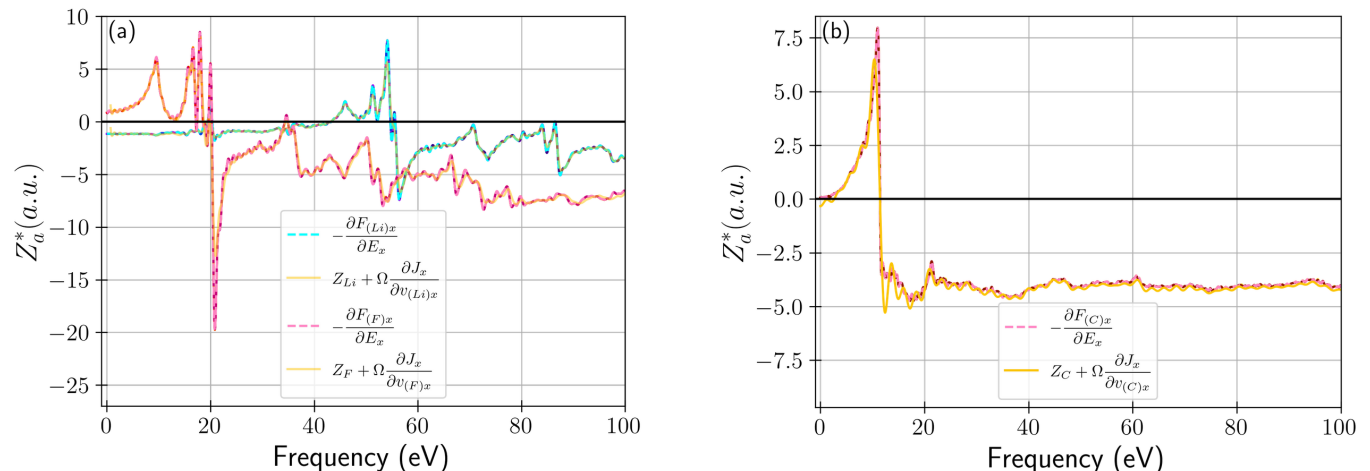


FIG. S2. Nonadiabatic Born Effective Charges  $Z_a^*$ : (a) 8-atom unit cell of LiF fcc crystal, and (b) 8-atom unit cell of C diamond, computed using two equivalent definitions of perturbation-response measures.

A real-time TDDFT-based dynamics, assuming fixed nuclear positions, of the system after an initial perturbation,  $\lambda$ , reveals the relaxation of the electronic system and the subsequent measure of Born effective charge tensor,  $Z_{ij}^*$ . A Gaussian smearing  $\gamma$  is used for Fourier transforming the signal to the frequency domain, *vide infra* for values. In Ref. [63] the authors use an instantaneous atomic displacement as the initial perturbation and calculated the time-dependent current response. This is based on the relationship:

$$\hat{Z}_a^* = Z_a \hat{I} + \frac{\partial \mathbf{P}}{\partial \mathbf{R}^a} \equiv Z_a \hat{I} + \frac{\partial \mathbf{J}}{\partial \mathbf{v}^a}, \quad \text{with} \quad (\text{S14})$$

$$\lambda \equiv \delta \mathbf{R}^a = \int dt \mathbf{v}^a(t) \delta(t),$$

where  $\mathbf{v}^a$  is the velocity of the ion,  $a$ . We propose the calculations based on the instantaneous macroscopic electric

field pulse:

$$\begin{aligned}\hat{Z}_a^* &= -\frac{\partial \mathbf{F}_a}{\partial \mathbf{E}}, \quad \text{with} \\ \lambda &\equiv \delta \mathbf{A} = \int dt \mathbf{E}(t) \delta(t).\end{aligned}\tag{S15}$$

This has the same advantage for calculation of nonadiabatic BEC as it does for the static BEC, the time-dependent propagation (or self-consistent DFPT) can be done for one perturbation, while calculating the observable many times. We validate our approach by comparing with certain calculations carried out in Ref. [63], namely ambient conditions lithium fluoride, and diamond, along with aluminium already included in the main text. This also allows us to compare the effect of using semi-core and frozen core pseudopotentials against the all-electron calculations in Ref. [63]. We calculate similar spectra compared to Ref. [63], with large deviations occurring only at large frequencies, where the effect of the pseudopotentials becomes prominent. We see excellent agreement between the two approaches for calculating  $\hat{Z}_a^*(\omega)$ , in both time (Fig. S1) and frequency domains (Fig. S2).

#### S4. TDDFT SIMULATION DETAILS

All simulations in the letter and these supplemental materials are performed via time-dependent Kohn-Sham density functional theory. We apply either fully deterministic or mixed stochastic-deterministic approaches, using the pseudopotential plane-wave DFT code **SHRED** (Stochastic and Hybrid Representation of Electronic structure by Density functional theory) developed by the authors at Los Alamos National Laboratory [52, 73]. Table S1 shows the parameters used to perform the simulations. We utilize the Short Iterative Lanczos propagation scheme [76], with no enforced time reversal symmetry. For section S3, we utilize Hartwigsen-Goedecker-Hutter (HGH) pseudopotentials from the **cp2k** database [77]. For the simulations presented in the letter, we utilize Optimized Norm-Conserving Vanderbilt pseudopotentials [78] (ONCV, version 3.2.3) from the PseudoDojo repository [79].

TABLE S1. Simulation parameters for the letter and supplemental materials. Key:  $\rho$  - total mass density,  $k_B T$  - electron temperature,  $N_\psi$  - number of deterministic Kohn Sham orbitals,  $N_\chi$  - number of complementary stochastic vectors, k-grid - Broullion Zone sample via Monkhorst-Pack grids (no  $\Gamma$ ) [80],  $N_a$  - number of atoms in unit cell, Ecut - maximum planewave energy defining basis and real-space grid,  $\gamma$  - the Gaussian dampening coefficient / broadening parameter,  $E_0$  - the perturbing electric field strength,  $dt$  the electronic time step.

| System         | $\rho$ [g/cm <sup>3</sup> ] | $k_B T$ [eV] | $N_\psi$ | $N_\chi$ | k-grid          | $N_a$       | Ecut [eV] | $\gamma$ [eV] | $E_0$ [a.u.] | $dt$ [a.u.] |
|----------------|-----------------------------|--------------|----------|----------|-----------------|-------------|-----------|---------------|--------------|-------------|
| -Letter-       |                             |              |          |          |                 |             |           |               |              |             |
| Al (FCC)       | 2.7                         | 0.025        | 14       | 0        | 16 × 16 × 16    | 4           | 500       | 0.136         | 0.01         | 0.05        |
| Al (FCC)       | 2.7                         | 1.0          | 28       | 0        | 16 × 16 × 16    | 4           | 500       | 0.136         | 0.01         | 0.05        |
| Al (FCC)       | 2.7                         | 3.0          | 42       | 0        | 16 × 16 × 16    | 4           | 500       | 0.136         | 0.01         | 0.05        |
| Al (FCC)       | 2.7                         | 5.0          | 84       | 0        | 16 × 16 × 16    | 4           | 500       | 0.136         | 0.01         | 0.05        |
| Al (WDM)       | 2.7                         | 1.0          | 224      | 0        | 2 × 2 × 2       | 64          | 500       | 0.015         | 0.01         | 0.05        |
| C (WDM)        | 0.5                         | 1.0          | 320      | 0        | $\Gamma$ -point | 64          | 987       | 0.272         | 0.01         | 0.022       |
| C (WDM)        | 3.52                        | 1.0          | 224      | 0        | 2 × 2 × 2       | 64          | 1000      | 0.272         | 0.01         | 0.021       |
| C-Be-H (WDM)   | 1.37                        | 5.0          | 1120     | 112      | $\Gamma$ -point | 128/128/128 | 1200      | 0.272         | 0.1          | 0.018       |
| -Supplemental- |                             |              |          |          |                 |             |           |               |              |             |
| Li-F (fcc)     | 2.53                        | 0.025        | 24       | 0        | 20 × 20 × 20    | 4/4         | 500       | 0.136         | 0.01         | 0.043       |
| C (Diamond)    | 3.53                        | 0.025        | 16       | 0        | 20 × 20 × 20    | 4           | 500       | 0.136         | 0.01         | 0.043       |